Appendix data: Alternation of formation dynamics and material structure during phase transformation from amorphous calcium phosphate to octacalcium phosphate using immobilized carboxylic-functional groups on gold nanoparticles

Yuki Sugiura, Kazuo Onuma, Masahiro Nagao and Atsushi Yamazaki

Experimental Method

Characterization of the $CaPO_4$ phases formed in the solutions containing reference gold nanoparticles and CGNs.

The treated materials, or their ultrathin cross sections prepared using a microtome, were each placed on an amorphous-carbon-coated Cu micro grid for TEM (JEM-2100, JEOL Co., Japan) observations. The phases of the materials were characterized according to their SAED patterns. The prepared ultrathin cross sections (~200 nm) were placed on a Cu micro-grid for cryo-HR-TEM observation. Cryo-HR-TEM observation was performed using a liquid-N_2 cryogenic holder (FE-TEM: Hitachi HF-3000S, Hitachi High Technologies Co., Ibaraki, Japan, FE-TEM, Tecnai G^2 20, FEI, the Netherlands) at acceleration voltages of 200 kV (JEM-2200 for TEM and Tecnai G^2 20 for cryo-HR-TEM) and 300 kV (HF-3000S for cryo-HR-TEM). The operating temperature of the cryo-HR-TEM observation was approximately −180 °C.

The Ca/PO_4 ratios of the ACP formed during the transformation stage and ratios of the precipitated crystalline phases during subsequent stages in the solutions containing the reference gold nanoparticles and CGNs were determined using energy dispersive X-ray spectroscopy (FE-SEM/EDX, FE-SEM: FEI40, FEI Co., the Netherlands; EDX: EDAX GENESIS, EDAX Japan Co., Japan).

Solid-state Raman spectra of the materials formed in the solutions were obtained via reflection-type microscopic Raman spectroscopy (InVia Micro Raman Spectroscopy, Renishaw Japan Co., Japan) with a semiconductor laser as the light source (λ_w = 785 nm). The samples were mounted on glass plates and placed in the spectrometer. All measurements were conducted in accumulative static mode, with a wavenumber resolution of ~0.5 cm^{-1}. The wavenumbers of all the spectra were calibrated using the Si spectral line (520.5 cm^{-1}) as a standard.

The ^{31}P chemical shifts in the $CaPO_4$s were determined using a solid-state NMR spectrometer (NMR: JNM-ECX400 JEOL Co., Japan, and AVANCE III HD 600WB, Bruker AXS Co., USA) with a resonance frequency of 400.0 MHz (JNM-ECX400) and 600 MHz (AVANCE III HD 600WB). For all these measurements, magic-angle spinning (MAS) with a single pulse mode for ^{31}P was applied at frequencies of 10000 or 15000 rpm in 4 or 5 mm zirconia rotors. The sample weight was ~0.2 g and the contact time for the ^{31}P MAS measurements was 36 ms with relaxation delays of 60 s or 5 ms with relaxation delays of 10 s in each measurement interval. The number of repetitions per measurement was 1400. The chemical shift of ^{31}P was calibrated as 0.0 ppm using a 0.5 M K_2HPO_4–KH_2PO_4 solution with a pH of 6.5.

XRD (RINT40, Rigaku Co., Japan, λ_w = 0.15406 nm) analyses were performed at

an acceleration voltage of 50 kV and a magnitude of 100 mA using a Cu target. The 2θ value was varied from 3° to 60° in 0.01° increments. The time required per step was 0.5 s. The entrance slit size was 5 mm × 10 mm.

Resulting Data

Characterization for reference gold nanoparticles and CGNs containing solutions by visible-light spectroscopy

Figure S1 shows visible-light absorption spectra of both solutions. The solution containing the reference gold nanoparticles was red, whereas that containing the CGNs was *sakura-iro* (a traditional pink similar to mauve Japanese color). The carboxylic-functional groups shifted the peak of the absorption spectrum from 515.5 nm (reference solution) to 518.5 nm (CGNs-containing solution). Because the wavelength can be resolved to below 0.5 nm, this shift in the absorbance peak is real.

Chemical composition of the ACP and precipitates determined using FE-SEM/EDX

Fig. S2 shows the Ca/PO_4 ratios of the ACP and precipitates formed at various stages in the reference and CGNs-containing solutions. The Ca/PO_4 ratios of the

materials taken from both the reference and CGNs-containing solutions increased gradually. The ratios for the ACP in both solutions were ~1.06 at 10 min and then rapidly increased, reaching ~1.25 prior to initial precipitation (~70 min and ~170 min in the reference and CGNs-containing solutions, respectively). After precipitation, the ratios of the precipitates in both solutions slowly increased and reached ~1.35 three days after starting the reactions.

TEM analysis of the materials precipitated in the reference and CGNs-containing solutions.

Fig. 7 shows TEM photographs of precipitates taken from the reference solution. The particles in the initial precipitate (~70 min) were roughly spherical, with diameters ranging from 2 to 5 μm (Fig. 7a), and were similar to those taken from the CGNs-containing solution after the same reaction period (Fig. 8a). Each sphere was composed of flexible plate-like crystals with width 100–200 nm (Fig. 7b). Cryo-HR-TEM observation showed well-arranged lattice fringes that coincided with an (002) *d*-spacing of 3.43Å in OCP unit cell (Fig. 7c). A TEM image of the OCP crystals in the reference solution at 12 h is shown in Fig. 7d. The typical plate-like morphology developed at the final reaction stage can be seen.

Fig. 8a shows a TEM photograph of the initial precipitates formed in the CGNs-containing solution during the initial precipitation period (~170 min). The particles were roughly spherical with diameters in the range from 2-5 μm. Each sphere was composed of flexible needle-like crystals with width 10–50 nm (see inset at upper right in Fig. 8a). Ultrathin cross sections of these spherulites (inset) showed that the needles were elongated along the direction from the core to the outer region. Fig. 8b shows a cryo-HR-TEM photograph of the initial precipitates formed in the CGNs-containing solution. The precipitates nearly completely consisted of complex lattice fringes such as those seen in Fig. 5h, which is in contrast to the initial precipitates formed in the reference solution (Fig. 7c). Well-arranged lattice fringe regions were also observed although they were rare (Fig. 8c). In Fig. 8c, we can see that none of the multiple lattice fringes crossed one other, which is necessary to unambiguously identify the crystallographic orientation of the material; however, the interspace distance of 3.17 Å between the neighboring fringes was coincident to that of the *d*-spacing of the (-521), orientation in the OCP unit cell.

After 1 day of solution preparation, the precipitates in the CGNs-containing solutions adopted the plate-like form typical of OCP crystals (upper right inset in Fig. 8d) similar to that observed in Fig. 7d. In addition, Laue spots corresponding to (002)

and (031) diffractions of single OCP crystals were clearly observed in the SAED pattern (Fig. 8d). In Fig. 8e, a cryo-HR-TEM photograph of the well-arranged lattice fringes of different OCP crystals observed after 1 day can be seen. Note that particular structures other than OCP were also observed in the crystal. Moreover, the lattice fringes were not only well-arranged but also often exhibited moiré patterns (Fig. 8e), and sometimes they were separated by complex lattice fringes (black arrow in Fig. 8f), similar to those observed in Fig. 8b. Furthermore, the well-arranged lattice fringes were observed in nearly all the plate-like crystals, whereas the complex lattice fringe pattern was observed only in a small fraction of the image.

In the reference solution, the initial precipitate formed as spherulites of plate-like crystals, and the cryo-HR-TEM image showed well-arranged lattice fringes. On the other hand, in the CGNs-containing solution, the initial precipitate formed as spherulites consisting of needle-like crystals, and the cryo-HR-TEM image showed a complex lattice fringe pattern. Hence, we concluded that the precipitate formed in the CGNs-containing solution had a looser structure relative to that formed in the reference solution.

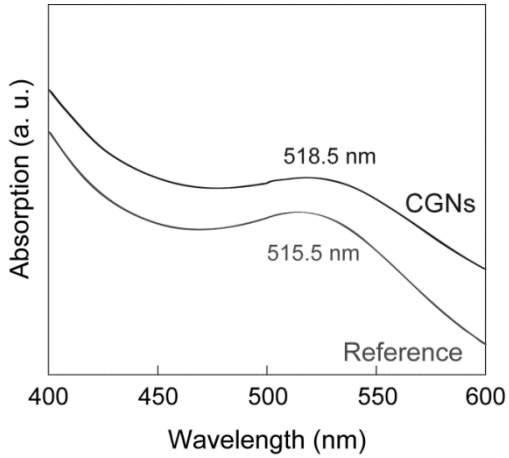

FIGURE. S1. Visible-light absorption spectra of the solution containing CGNs (black line) and reference gold nanoparticles (grey line).

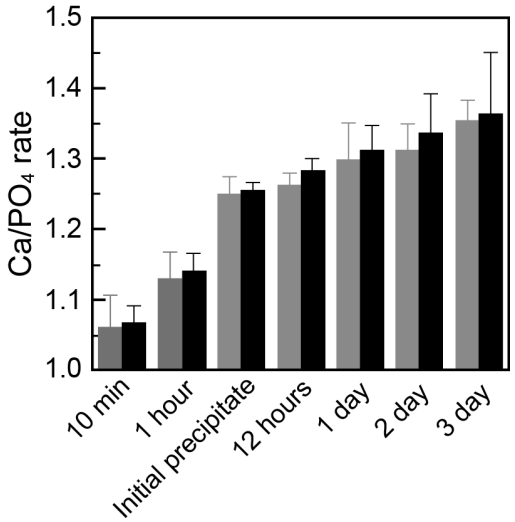

FIGURE. S2. FE-SEM/EDX data for the Ca/PO_4 ratios of the materials formed in the reference (grey bar) and CGNs-containing (black bar) solutions at various reaction stages.

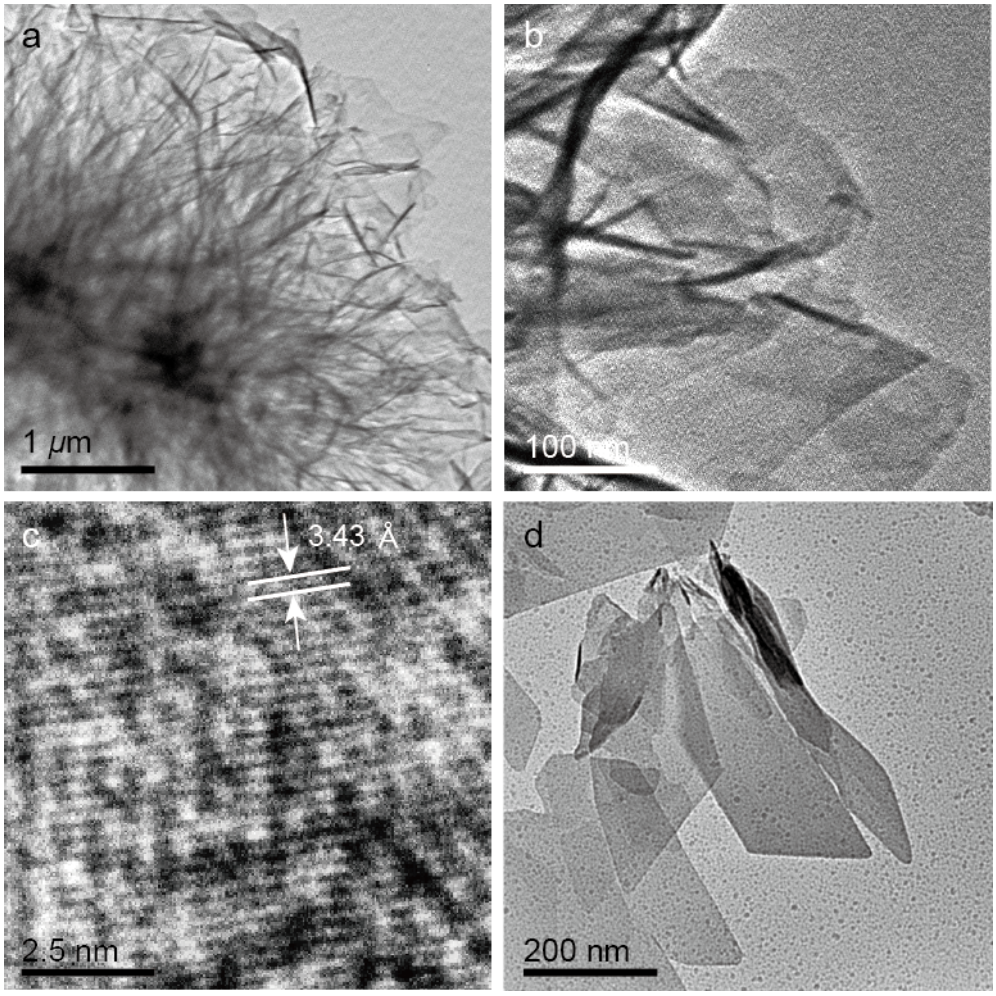

FIGURE. S3. TEM photographs of the precipitates formed in the reference solutions (200 kV). (**a**) TEM photograph of the initial precipitate. (**b**) Magnified image of (**a**). (**c**) Cryo-HR-TEM photograph of the well-arranged lattice fringes in the initial precipitates. (**d**) TEM photograph of the OCP plate-like crystals formed at 12 h.

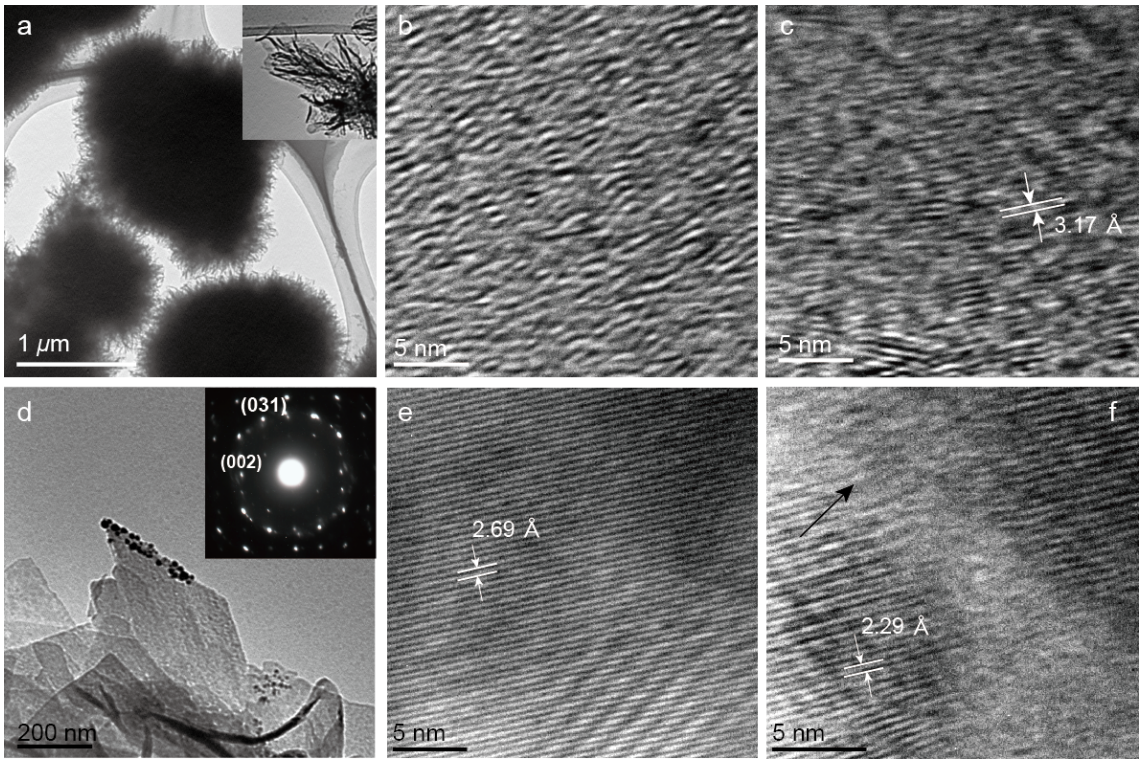

FIGURE. S4. TEM photographs of the precipitates formed in the CGNs-containing solution (300 kV). (**a**) TEM photograph of the initial precipitate (a magnified image is shown in the upper left). (**b**) Cryo-HR-TEM photograph of the complex lattice fringe region for the initial precipitate. (**c**) Cryo-HR-TEM photograph of the partially well-arranged lattice fringes in the initial precipitate. (**d**) TEM photograph with the SAED pattern of the precipitates formed after 1 day. The particles observed at the edges of the plate-like crystals are the gold nanoparticles. (**e**) Cryo-HR-TEM photograph of the precipitates formed after 1 day. Well-arranged lattice fringes and moiré fringes (lower right) are observed. (**f**) Cryo-HR-TEM photograph of the separated well-arranged lattice fringes. The black arrow indicates the region of the complex lattice fringes.